Soot volume fraction measurements over laminar pool flames of biofuels, diesel and blends

B. Tian[a,], C. T. Chong[b], L. Fan[a], J.-H. Ng[c], C. Zhang[a], S. Hochgreb[a]

[a] *Department of Engineering, University of Cambridge, Trumpington Street, CB2 1PZ Cambridge, UK*
[b] *UTM Centre for Low Carbon Transport in cooperation with Imperial College London, Universiti Teknologi Malaysia, 81310 Skudai, Johor, Malaysia*
[c] *Faculty of Engineering and the Environment, University of Southampton Malaysia Campus (USMC), 79200 Iskandar Puteri, Johor, Malaysia*

Abstract

Biodiesel and blends with petroleum diesel have shown their potential as renewable alternative fuels for engines, with additional benefits of low particulate matter and low sulfate emissions. In this paper we measure the soot volume fraction produced by three different methyl esters processed biodiesels (extracted from palm (PME), soy (SME) and coconut (CME)), and their blends with petroleum diesel, in a series of co-flow stabilized laminar pool flames, using laser induced-incandescence (LII) and laser extinction optical methods. The soot volume fraction measurement results show that all neat biodiesels produce only up to 33% of the total soot volume compared to pure diesel, and that the total soot volume correlates directly with the degree of unsaturation of the biodiesels. Blending leads to approximately linear behaviour of total soot volume, with a shift in slope with smaller sensitivity towards neat diesel.

Email address: bt312@cam.ac.uk (B. Tian)

Keywords: Biodiesel, Soot, Laser induced incandescence, Laser extinction

1. Introduction

A variety of industrially processed bioderived fuels have been introduced as replacements for diesel fuel, such as palm, rapeseed, coconut and soy. These are processed and tailored as a replacement for diesel, with suitably low cetane numbers, and viscosities adjusted as additives for appropriate operation in existing engines. These replacement fuels typically have 10-15% oxygen as elemental composition, which offers an additional benefit in the form of lower soot emissions, with some variations on the effect on NO_x [1]. A typical biodiesel consists of a mixture of monoalkyl esters of long-chain methyl esters produced via the transesterication process, in which the triglycerides contained in vegetable oils and animal fats react with methanol to form methyl esters and glycerol [2]. The chemical oxidation and soot formation pathways of biodiesel have been investigated in a number of studies [3, 4]. Although many studies have been produced in engines, fewer measurements have been made in well controlled devices suitable for model comparisons, such as vaporised laminar co-flow diffusion flames [5, 6], counterflow diffusion flames [7], spray flames [8], high pressure injection constant volume combustion chambers [9, 10] and wick-fed lamp diffusion flames [11]. Nerva *et al.* [10] studied the soot formation of soy biodiesel using soot extinction, laser induced incandescence (LII) and luminosity at pressures up to 6.7 MPa and 1000 K. The soot concentration for biodiesel was found to be lower by an order of magnitude compared to diesel, highlighting the role of oxygen and molecular structure of biodiesel in reducing sooting propensity. In a similar

but separate study [9], soy biodiesel was found to yield a higher value of soot mass fractions compared to butanol. Unlike diesel, butanol is a relatively short alcohol chain dthat shows low sooting propensity. The effect of oxygen concentration in the vessel was also investigated. The flame luminosity and soot production were shown to decrease with decreasing oxidizer content in the mixture, whereas higher ambient temperatures in the chamber increased soot production. The propensity of sooting for model biodiesels has been studied by Feng *et al.* [7] in a non-premixed counter-flow flame configuration using biodiesel surrogates, in the form of fatty acid esters. The model biodiesel fuels were shown to produce signicantly lower soot levels compared to the corresponding n-alkanes with similar carbon number. Interestingly, unsaturated methyl ester (methyl-crotonate: $C_5H_8O_2$) was shown to exhibit higher sooting propensity compared to the corresponding saturated methyl ester (methyl-butanoate: $C_5H_{10}O_2$), indicating that the effect of the unsaturation level in biodiesel on soot formation could be prominent. This is in agreement with results from an engine test operated using linseed biodiesel: this fuel with a higher unsaturation level emitted higher particulate matter and hydrocarbons compared to the less unsaturated palm biodiesel [12].

Kholgy *et al.* [5] measured the soot volume fraction of a biodiesel surrogate consisting of 50% n-decane/50% methyl-octanoate (as a surrogate for methyl oleate) in an co-flow diffusion flame, using the laser extinction method. The results were used as validation target for chemical kinetic models. Their computational study showed that the soot volume fraction and temperature profiles for the biodiesel surrogate are similar to that of n-decane, indicating a negligible effect of ester moiety on soot formation. The

result shows the low degree of unsaturation in biodiesel, rather than oxygen composition, may play the main role in lowing soot formation. Merchan-Merchan *et al.* [6] used a similar setup and measurement technique to investigate the extent of soot formation in the case of soy and canola biodiesels. Both biodiesels exhibited similar flame temperatures and soot volume fraction profiles. Tran *et al.* [11] investigated the sooting behaviour of soybean biodiesel/diesel blends using LII over a wick-fed lamp, showing that the biodiesel produced significantly lower soot, and that the variation was proportional to the blended fraction. Finally, Tran *et al.* [13] considered the burning and emission characteristics of biodiesels over a pool fire, but no soot measurements were made.

The present study addresses the following needs: (a) to provide absolute measurements of soot volume fraction over a controlled laminar pool fire of a known fuel; (b) to contrast the formation of soot over a pool fire for a range of biofuels with different degrees of unsaturation and for a range of blending conditions with diesel fuel.

Extinction-calibrated LII has been proven to be a robust non-intrusive method for soot volume fraction (f_v) measurement in flames [14–16]. However, in high soot loading environments, LII suffers from significant signal trapping [17]. To tackle the problem, a deconvolution method was used in the present study to correct the 2D LII images and provide quantitative measurements for future studies.

2. Methodology

2.1. Experiment

Figure 1 shows the co-flow stabilized laminar pool burner used in the present study. The burner consists of a co-flow tube (D = 96.8 mm), a stainless steel fuel cup (D = 20 mm, depth = 20 mm, wall thickness = 2.5 mm) and a holder for the cup. The dimensions of the cup and holder are shown in Fig. 1. A ceramic heating plate (CHP, D=24 mm, 12V, $\leq$ 240 °C) is used underneath the pool to keep a constant temperature of the fuel around 120 °C. A co-flow air of 18.2 cm/s is added around the fuel pool to reduce the flickering of the flame. The biodiesels tested in this work are methyl

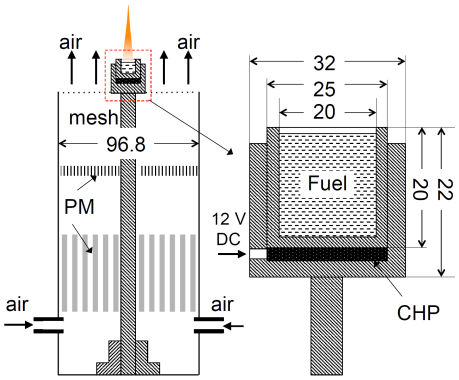

Figure 1: Co-flow stabilised laminar pool fire burner. CHP: ceramic heating plate; PM: porous material. Units in mm. Dimensions in mm, not to scale.

esters (ME) produced via a transesterification process from the feedstock of palm, soy and coconut oils, and are denoted as PME, SME and CME respectively. The composition of the biodiesels is measured using a standard Gas Chromatograph using a gas chromatograph (GC, Agilent 7620A) based on EN14103 standard, and listed in Table 2. The measured average formula of PME, SME and CME are: $C_{18.1}H_{34.9}O_{2.0}$, $C_{18.8}H_{34.5}O_{2.0}$ and $C_{13.5}H_{26.9}O_{2.0}$,

respectively. All biofuels tested contain $\geqslant$10% (mass fraction) of oxygen, and have a relatively low overall degree of unsaturation ($\leqslant$1.51), and are thus are naturally expected to yield lower soot emissions. The behaviour of soot over

	PME	SME	CME
C8:0	0	0	6.78
C10:0	0	0	5.61
C12:0	0	0	51.00
C14:0	0.93	0	18.51
C16:0	39.85	11.62	9.26
C18:0	3.55	4.51	1.66
C18:1	43.14	23.03	6.06
C18:2	12.53	54.22	1.12
C18:3	0	6.62	0
Unsaturation	0.62	1.51	0.08
Avg. C chain	17.1	17.8	12.5
MW (g/mol)	284.3	291.5	221.2
ΔH (MJ/kg)	37.3	37.0	35.2
H	12.29	11.84	12.18
C	76.46	77.18	73.36
O	11.25	10.98	14.46

Table 1: Top section: Composition (mass percentage) of biodiesels measured using GCMS. C8:0 means the main chain of eight carbon atoms with zero C=C double bonds. Bottom section: Properties and elemental mass percentage of biodiesels. The degree of unsaturation is calculated by multiplying the mass fraction of each species times the associated number of C=C double bonds. Heat values ΔH are from Ref. [18].

pool flames was investigated for a series of biodiesels and their blends with petroleum diesel (D100). The blends are indicated by the initial of the biofuel (P, S or C) and the percent by mass used in the mixture, *e.g.* P20 refers to 20% by mass in palm oil biodiesel. In all tests, the co-flow air flow velocity is kept at 18.2 cm/s. The fuel consumption rate of each case is measured by weighing the fuel burned over 10 min stable combustion, resulting in values

between 0.085-0.097 g/min.

The 2D LII measurements were performed using an similar set-up to that in Ref. [16]. The laser source is a 532 nm Nd:YAG laser (Litron nanoPIV) firing at 10-25 Hz. The laser beam is collimated into a parallel sheet by a series of beam shaping optics, followed by an aperture to generate a verified top-hat profile. The LII signal induced by the laser sheet was captured by an ICCD camera (LaVision Nanostar 1024 $\times$ 1280 pixels), fitted with a lens (Nikon AF Micro Nikkor 60 mm, f/5.6) and a band filter (Thorlabs FB400-40, central $\lambda = 400 \pm 8$ nm, FWHM = 40 nm) which minimises the luminosity from PAH fluorescence, C_2 and flame radiation. A delay of 20 ns was applied to the intensifier gate to avoid the interference of PAH LIF and residual laser scatter. A relatively short intensifier gate width of 30 ns was used to avoid bias towards larger particles [19]. The laser fluence used in the LII measurement was carefully selected. Figure 2 shows the dependence of the LII signal on the fluence of the laser sheet for the highest soot producing cases D100, P100, S100 and C100. The LII signal at each fluence represents the average value of 200 images at 20 Hz after background subtraction, obtained from the signal intensity between 0 to 35 mm height above the burner (HAB). The fuel pool surface is kept 1 mm below the cup lip before each measurement, and during the 10 second measurement, no significant decrease of the fuel surface level is observed as the fuel consumption rate is small (<0.1 g/min). All values are normalized using the maximum value of the case for purposes of locating the signal peak. In all cases, the LII signal rises rapidly with increasing laser fluence, as the temperature of the particles increase, reaching the sublimation point and an approximately fixed temperature and

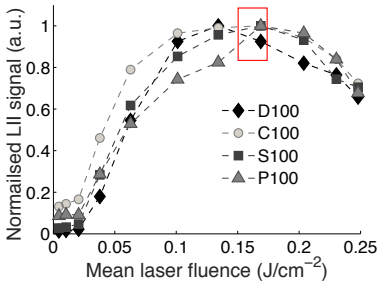

Figure 2: Fluence dependence of the LII signal for four unblended cases as a function of the fluence of laser sheet; the peak or plateau region (in the *marked rectangle*) is selected for the LII measurements. The values of LII signal intensities of each case are normalised using by maximum value for each fuel.

signal at a fluence around 0.15 J/cm^2, as indicated in the marked rectangle. In this region, the LII signal is less sensitive to local laser fluence, which allows a simplified description of the signal. In this work, we assume that the fluence dependence of LII signal of all blended cases is similar to the pure fuel cases, as their response curve should be somewhere in between the pure fuel cases. Figure 3 shows the beam profile and variance averaged over 200

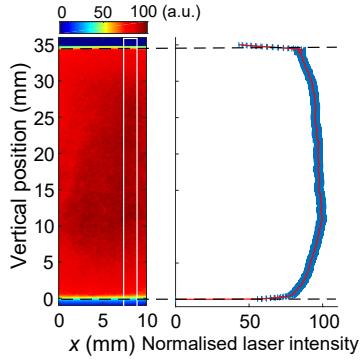

Figure 3: Normalised laser beam intensity profile used for LII excitation. Left: Rhodamine 6G fluorescence excited by laser sheet in a cuvette; right: integrated fluorescent light intensity profile over the region (red line) over the rectangle marked with a white border. Blue error bars indicate the signal variance shot-to-shot.

shots at 20 Hz, as characterised by the resulting fluorescence in a cuvette

containing Rhodamine 6G dye. The local intensity fluctuation of the laser sheet as represented by the standard deviation is lower than 5%, and the corresponding error introduced by fluctuations in spatial fluence is smaller than 3%. All images are averaged after background noise subtraction. The nominal spatial resolution is 50 μm/pixel for an imaging area of 35×35 mm^2.

2.2. LII calibration and correction

Laser extinction measurements are performed for a quantitative calibration of the LII signal [14]. A diode laser (Omicron LuxX-638-150, 638 nm wavelength) is used as laser source for extinction. The laser beam intensity ahead and behind soot absorption, I_0 and I_t, respectively, are determined using photodiodes (Thorlabs SM05PD1A Silicon Photodiode, 350-1100 nm). The extinction ratio of the laser beam $A = I_t/I_0$ can be expressed as [14, 16]:

$$A = \frac{I_t}{I_0} = \exp\left(-\int K_e \, \mathrm{d}x\right) \tag{1}$$

where x is the path length across the sampling region, and K_e is the extinction coefficient. The extinction coefficient K_e can be related to the local soot volume fraction f_v in the Rayleigh regime (particle smaller than wavelength) as:

$$K_e = \frac{6\pi E(m)}{\lambda_e} f_v \tag{2}$$

where $E(m)$ is the absorption function of soot $E(m) = \text{-Im}\left(\frac{m_e^2-1}{m_e^2+2}\right)$ and m_e is the complex refractive index of soot at the extinction wavelength λ_e (638 nm).

The local value of f_v can be determined in the axisymmetric system by spatial differentiation of the total absorption factor A, which is a function

of chord distance x, obtained at the centreline of the flame via inverse Abel transform [14, 16]:

$$f_v(r) = \frac{\lambda_e}{6\pi^2 E(m)} \int_x^\infty \frac{[\ln A(x)]'}{\sqrt{x^2 - r^2}} \mathrm{d}r \tag{3}$$

where r is the radial distance. In the present study, the location HAB=25 mm in D100 flame is selected to conduct extinction measurements, as this is close to the location of maximum integrated LII signal $\int S_m \, dx$. The f_v value is then calibrated from the measured LII signal intensity S_m by assuming that the LII and extinction signals are linearly proportional (as detailed in the following sections).

No reduction of LII signal is observed along the propagation direction of the laser sheet, indicating the whole probe volume is in the plateau region of LII measurement (Fig. 2), and a correction for the attenuation of the laser sheet is considered unnecessary. However, because the flames in the present study produce relatively high soot concentrations, the LII signal collected is subject to trapping as it travels from the excitation plane to the camera, and a correction on the signal trapping is necessary before the calibration [17]. Since the flame is axisymmetric, the attenuation of the LII signal in the flame due to signal trapping (as a function of x) can be estimated from the absorption ratio obtained for the extinction measurement along chord distance x. In the present study, we measured A at HAB=25 mm for D100 along x over a step distance of 0.25 mm from $x = -5$ mm to 5 mm, generating a well-resolved $A(x)$. By combining Eqs. (1) and (2) and considering that the LII absorption only occurs through one half of the symmetric flame, the

corrected LII signal $S(x)$ can be obtained from the measured signal $S_m(x)$:

$$S\left(x\right) = S_m\left(x\right) A(x) \exp\left(-\frac{\lambda_e E(m_L)}{2\lambda_s E(m_e)}\right) = S_m K_c(x) \tag{4}$$

where $K_c(x)$ is the correction constant; m_L and m_e are calculated at 400 nm and 638 nm, respectively, to account for the different absorption ratios at the two wavelengths. Values of $E(m)$ at the two wavelengths are taken as 0.41 and 0.27, respectively, referred to the latest review in [20] using a RDG-FA model corrected for internal multiple scattering effects. The LII signal at HAB=25 mm in D100 flame can finally be calibrated using the extinction data by considering that the integrated f_v across the centerline chord at a certain HAB yields a total logarithmic attenuation. We assume that the corrected LII signal S is proportional to the soot volume fraction with a linear coefficient, such that $S = Cf_v$ [14, 16, 21], so that at the flame centerline, we have:

$$\ln\frac{I_t}{I_0} = \frac{6\pi E(m_e)}{\lambda_e}\frac{1}{C}\int_{-\infty}^{+\infty} S(r)\ \mathrm{d}r \tag{5}$$

The calibration constant C is therefore determined using Eq. (5), whose value is 2.9156×10^8 at HAB=25 mm in D100 flame. This value of C is assumed to remain the same for all flames, since the soot produced by different liquid fuels shares similar optical properties [22] and the imaging parameters are kept unchanged throughout the experiment. A correction and calibration method for all other cases is then possible, using the known value of C, with f_v as the only unknown variable, and one value of A for the chord centerline

at the same reference point. Considering the at a fixed chord position x at in flame center, $r = x$, $S_m(x) = S_m(r)$, we have:

$$Cf_v(r) = S_m(r) \exp\left(-\frac{12\pi E(m_L)}{\lambda_s} \int_0^\infty \frac{r f_v(r)}{\sqrt{r^2 - x^2}}\, \mathrm{d}r\right) \tag{6}$$

The exponential factor represents the attenuation of the LII signal expressed in Eq. (4). By discretizing a cross section at a particular height of the flame into a series of concentric rings, and numbering the values from i=0 to N, the Eq. (6) can be written as:

$$Cf_v(i) = S_m(i) \exp\left(-\frac{6\pi E(m_L)}{\lambda_s} \sum_{j=i}^{N} f_v(j)\Delta_{i,j}\right) \tag{7}$$

where $\Delta_{i,j}$ is given by Eq. (8) by assuming the distance between two adjacent rings (pixels) is δ:

$$\Delta_{i,j} = \begin{cases} \delta\left(\sqrt{j^2 - i^2} - \sqrt{(j-1)^2 - i^2}\right), i < j \leqslant N \\ 0,\ j \leqslant i \end{cases} \tag{8}$$

For $i = N$, the signal is emitted from the outermost ring, which is considered as unattenuated: $S(N) = S_m(N)$, so we have $f_v(N) = S_m(N)/C$. For other rings from $i = N-1$ to $i = 1$, as the term $f_v(i)$ is the only unknown variable in Eq. (7) and appears in both sides of the equation, and can therefore be solved for iteratively in descending order from $i = N - 1$ to $i = 1$.

3. Results and discussion

Both corrected and uncorrected f_v profiles at HAB=25 mm for the D100 flame are shown in Fig. 4 and compared with the extinction data. The value of the correction constant K_c is obtained by extinction measurements in 0.25 mm steps along the radius (described in Section 2.2) and interpolated to a resolution of 50 μm to correct S_m. The data shows that signal trapping causes about 14% underestimation of f_v at the flame center, and less than 5% at the edges. Figure 5 shows the natural luminosity of all tested flames and

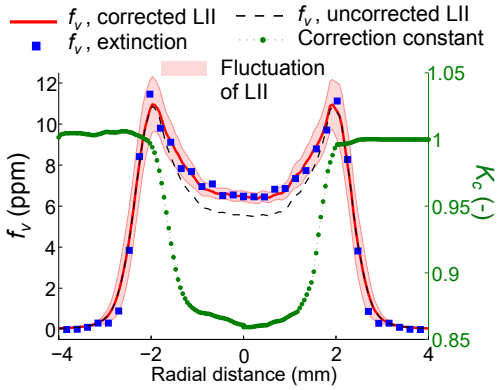

Figure 4: Corrected (red line with pink shaded fluctuation region) and uncorrected (dashed line) f_v profile at HAB=25 mm of D100 flame, compared to values obtained from extinction f_v (blue squares), and correction coefficient K_c (green dots). K_c is obtained by moving the extinction measurement in 0.25 mm steps and interpolated to the resolution of 50 μm.

the corresponding f_v map from HAB=0 to 35 mm. The fuel consumption rate for each case is noted on each flame photo. The fuel consumption rate is within 7% for all 16 cases, but the visible flame heights are widely different, from 25 mm to more than 80 mm (sooting flames). All pure biodiesel visible flame heights are similar, and shortest in height, increasing approximately linearly towards the highest visible heights of the pure diesel. In the latter

case (D100), the flame emits visible unburned soot from the flame tip, so the flame height is not very well defined, as is the case for 20% and 40% addition of all three biodiesels. Beyond 60% biofuel fraction or more, the flames no longer emit soot, which means that any soot produced is oxidized within the flame. The f_v maps for all cases are shown in Fig. 5 (rows 2 and 4). An obvious decrease in f_v with biodiesel addition can be observed in all three series of flames, which is consistent with the expectation of oxygen containing biodiesels [18]. The underlying data is reported as supplemental material (Fig. S1) for ease of use by models. The spatial profiles of f_v at

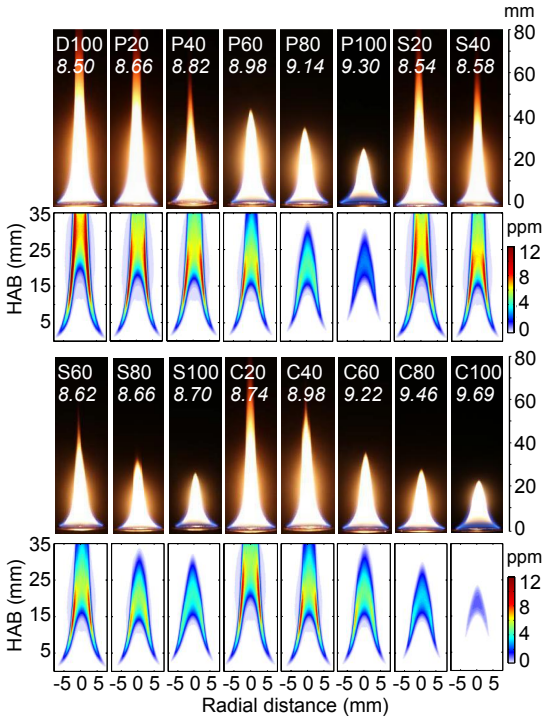

Figure 5: Natural luminosity of tested flames and corresponding f_v map from HAB=0 to 35 mm. The fuel consumption rate of each case is noted on each subfigure in units of 10^{-2} g/min.

HAB=25 mm for all cases are compared in Fig. 6. The profile of D100

is plotted using red dashed lines in each sub-figure as a reference. At a particular height, the values of f_v replicate a similar linear behavior as the maximum f_v against the blend ratio of biofuels. The profiles indicate that for cases with biodiesel ratios lower than 60%, at this particular height, the maximum f_v appears in the annular region, in contrast with cases with high biodiesel ratio (80% and 100%), where the maximum f_v appears along the flame centerline.

The appearance of soot depends on the residence time of the fuel within a fuel-rich region at high temperatures. The heating value of the three fuels are similar, and all about 15% percent lower than petroleum diesel [18]. The expected adiabatic temperatures for the different fuels are within 35 K based on the heating values and equilibrium calculations. In the case of D100, soot is promptly formed at high temperatures near the base of the flame after a short residence time, and continues as the heat is transferred towards the centerline of the flame. More soot results near the high temperatures at the edge than from the cooler centerline. In the case of the oxygenated biodiesels, the high temperatures at the base are insufficient to produce sufficient soot fractions over a short residence time. Only after sufficient residence time at high temperatures, away from oxidiser does the biodiesel pyrolysis create sufficient soot at the centerline. At higher HABs, after sufficient residence time at high temperatures all soot profiles converge to maxima at the centerline, as shown in Fig. 5. The maximum soot volume fraction for each case is shown in 7, as a function of biodiesel mass fraction. CME and all of its blends with petroleum diesel produces the least f_v, while SME produces the most, certainly beyond the 40% blending ratio. This observation is consis-

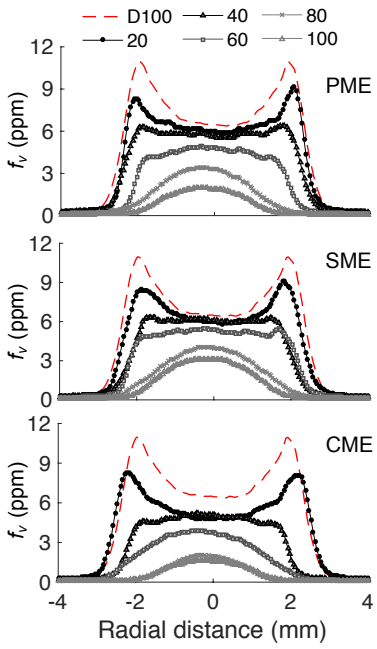

Figure 6: Profile of f_v at HAB=25 mm for three series of flames. D100 is plotted using red dashed lines in each sub-figure as reference.

tent with the fact that CME has the most saturated bonds in biodiesel (93%) among the three tested fuels, compared with SME, whose saturated composition mass ratio is only about 16%. Over a blend ratio from 0 to 80%, the maximum f_v is reduced by a factor of about 2.9 for CME, 2.2 for PME and 1.7 for SME, showing the addition of biodiesel can significantly suppress the formation of soot. A parallel comparison among three biodiesels shows the degree of unsaturation is a key factor for soot formation in tested flames. The highly saturated CME (degree of unsaturation 0.08) produces only 22.4% of maximum f_v compared with SME (degree of unsaturation 1.51) in pure form, and in almost all blended cases. CME blend produces the least soot, while SME produces the most. One exception to this trend happens when the mass blend ratio is 20%, and the maximum f_v in P20 is slightly higher than that of S20. This is yet not explained in the current research. The measurements were repeated 3 times; the results are all very close to each other, with 2 values showing S20 is slightly higher, and one where P20 is higher. A final

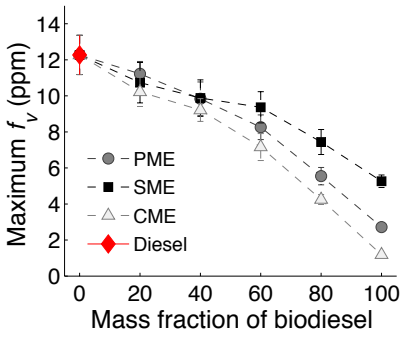

Figure 7: Maximum f_v as a function of biodiesel mass fraction.

comparison can be made by considering the soot flux in the axial direction,

which should scale as

$$\dot{V}_s = 2\pi \int r f_v u \, \mathrm{d}r \tag{9}$$

where u is the mean axial velocity through the profile. The heating value of all biofuels is similar, and about 10-15% lower than that of D100 [18], and the fuel mass consumption rates are within 10%. Therefore it is reasonable to assume that the value of u is not significantly different. In that case, the total *relative* mean soot flux going into the flame region is represented by a total area weighted soot volume fraction $\bar{f}_v$, as a function of height above the burner, (Fig. 8). As expected, the mean soot volume fraction ranks in a similar way as the maximum f_v plots. However, the mean value goes to zero for the biofuels across the flame, the D100 (and the blends above 40% biofuel, not shown) have a non-zero soot flux at the top of the image.

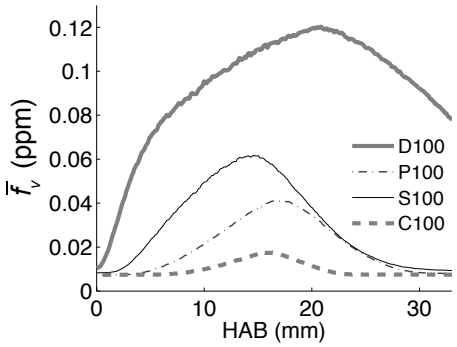

Figure 8: Normalised mean soot volume fraction $\frac{1}{\pi R^2}\int_0^R 2\pi r f_v(r)\mathrm{d}r$ in D100, P100, S100 and C100 flames, where R is the radius of the pool.

4. Conclusion

Extinction calibrated laser induced incandescence (LII) is applied to measure the soot volume fraction in laminar pool fires fueled with three different

biodiesels (PME, SME and CME) and their blends with petroleum diesel. The biodiesels have similar elemental composition but different degrees of unsaturation. The measured levels of maximum and total volume integrated over the image show that peak soot volume fractions produced by neat biofuels in this situation are 10.6 to 32.6% that of diesels, and that the fuel soot production ranks in order of degree of unsaturation. Blending leads to lower soot values, although the value is not linear across the entire range, with a slower reduction in total soot amount for blending of small quantities of biodiesel, followed by a faster decrease towards neat biofuel.

Acknowledgements

B. Tian is funded through a fellowship provided by ZEPI. C. Zhang is funded through a fellowship provided by CSC. The authors gratefully acknowledge the financial support from Universiti Teknologi Malaysia under grant number RG84263, and a Newton Advanced Fellowship (NA160115) for C. T. Chong.

References

[1] M. Lapuerta, O. Armas, J. Rodriguez-Fernandez, Progress in Energy and Combustion Science 34 (2008) 198 – 223.

[2] J. V. Gerpen, Fuel Processing Technology 86 (2005) 1097 – 1107. Biodiesel Processing and Production.

[3] O. Herbinet, W. J. Pitz, C. K. Westbrook, Combustion and Flame 154 (2008) 507 – 528.

[4] J. P. Szybist, J. Song, M. Alam, A. L. Boehman, Fuel Processing Technology 88 (2007) 679 – 691. Biofuels for Transportation.

[5] M. R. Kholghy, J. Weingarten, M. J. Thomson, Proceedings of the Combustion Institute 35 (2015) 905–912.

[6] W. Merchan-Merchan, S. McCollam, J. F. C. Pugliese, Fuel 156 (2015) 129–141.

[7] Q. Feng, A. Jalali, A. M. Fincham, Y. L. Wang, T. T. Tsotsis, F. N. Egolfopoulos, Combustion and Flame 159 (2012) 1876–1893.

[8] C. Allouis, M. Romano, F. Beretta, L. Viegas, a. D'Alessio, Combustion Science and Technology 134 (1998) 457–475.

[9] H. Liu, C. F. F. Lee, M. Huo, M. Yao, Energy and Fuels 25 (2011) 3192–3203.

[10] J.-G. Nerva, C. L. Genzale, S. Kook, J. M. García-Oliver, L. M. Pickett, International Journal of Engine Research 14 (2013) 373–390.

[11] M. K. Tran, D. Dunn-Rankin, T. K. Pham, Combustion and Flame 159 (2012) 2181–2191.

[12] M. Salamanca, F. Mondragon, J. R. Agudelo, P. Benjumea, A. Santamaria, Combustion and Flame 159 (2012) 1100–1108.

[13] V. Tran, C. Morton, R. N. Parthasarathy, S. R. Gollahalli, International Journal of Green Energy 11 (2014) 595–610.

[14] C. R. Shaddix, K. C. Smyth, Combustion and Flame 107 (1996) 418–452.

[15] H. A. Michelsen, C. Schulz, G. J. Smallwood, S. Will, Progress in Energy and Combustion Science 51 (2015) 2–48.

[16] B. Tian, Y. Gao, S. Balusamy, S. Hochgreb, Applied Physics B 120 (2015) 469–487.

[17] F. Liu, K. a. Thomson, G. J. Smallwood, Applied Physics B 96 (2009) 671–682.

[18] S. K. Hoekman, A. Broch, C. Robbins, E. Ceniceros, M. Natarajan, Renewable and Sustainable Energy Reviews 16 (2012) 143 – 169.

[19] E. Cenker, G. Bruneaux, T. Dreier, C. Schulz, Applied Physics B 118 (2015) 169–183.

[20] A. Bescond, J. Yon, F. X. Ouf, C. Rozé, A. Coppalle, P. Parent, D. Ferry, C. Laffon, Journal of Aerosol Science 101 (2016) 118–132.

[21] F. Liu, G. J. Smallwood, Applied Physics B 112 (2013) 307–319.

[22] S. S. Krishnan, K.-C. Lin, G. M. Faeth, Journal of Heat Transfer 123 (2001) 331.

List of supplementary files

Figure S1. Soot volume fraction f_V distribution (data-readable TIFF figure) in all tested cases.

List of figure captions

Figure 1. Co-flow stabilised laminar pool fire burner. CHP: ceramic heating plate; PM: porous material. Units in mm. Dimensions in mm, not to scale.

Figure 2. Fluence dependence of the LII signal for four unblended cases as a function of the fluence of laser sheet; the peak or plateau region (in the *marked rectangle*) is selected for the LII measurements. The values of LII signal intensities of each case are normalised using by maximum value for each fuel.

Figure 3. Normalised laser beam intensity profile used for LII excitation. Left: Rhodamine 6G fluorescence excited by laser sheet in a cuvette; right: integrated fluorescent light intensity profile over the region (red line) over the rectangle marked with a white border. Blue error bars indicate the signal variance shot-to-shot.

Figure 4. Corrected (red line with pink shaded fluctuation region) and uncorrected (dashed line) f_v profile at HAB=25 mm of D100 flame, compared to values obtained from extinction f_v (blue squares), and correction coefficient K_c (green dots). K_c is obtained by moving the extinction measurement in 0.25 mm steps and interpolated to the resolution of 50 μm.

Figure 5. Natural luminosity of tested flames and corresponding f_v map from HAB=0 to 35 mm. The fuel consumption rate of each case is noted on each subfigure in units of 10^{-2} g/min.

Figure 6. Profile of f_v at HAB=25 mm for three series of flames. D100 is plotted using red dashed lines in each sub-figure as reference.

Figure 7. Maximum f_v as a function of biodiesel mass fraction.

Figure 8. Normalised mean soot volume fraction $\frac{1}{\pi R^2}\int_0^R 2\pi r f_v(r)\mathrm{d}r$ in

D100, P100, S100 and C100 flames, where R is the radius of the pool.

Tables

	PME	SME	CME
C8:0	0	0	6.78
C10:0	0	0	5.61
C12:0	0	0	51.00
C14:0	0.93	0	18.51
C16:0	39.85	11.62	9.26
C18:0	3.55	4.51	1.66
C18:1	43.14	23.03	6.06
C18:2	12.53	54.22	1.12
C18:3	0	6.62	0
Unsaturation	0.62	1.51	0.08
Avg. C chain	17.1	17.8	12.5
MW (g/mol)	284.3	291.5	221.2
ΔH (MJ/kg)	37.3	37.0	35.2
H	12.29	11.84	12.18
C	76.46	77.18	73.36
O	11.25	10.98	14.46

Table 2: Top section: Composition (mass percentage) of biodiesels measured using GCMS. C8:0 means the main chain of eight carbon atoms with zero C=C double bonds. Bottom section: Properties and elemental mass percentage of biodiesels. The degree of unsaturation is calculated by multiplying the mass fraction of each species times the associated number of C=C double bonds. Heat values ΔH are from Ref. [18].